ACS Catalysis

pubs.acs.org/acscatalysis

Research Article

Nature of the Active Sites on Ni/CeO_2 Catalysts for Methane Conversions

Pablo G. Lustemberg, Zhongtian Mao, Agustín Salcedo, Beatriz Irigoyen, M. Verónica Ganduglia-Pirovano,* and Charles T. Campbell*

Cite This: *ACS Catal.* 2021, 11, 10604−10613

Read Online

ACCESS | Metrics & More | Article Recommendations | Supporting Information

ABSTRACT: Effective catalysts for the direct conversion of methane to methanol and for methane's dry reforming to syngas are Holy Grails of catalysis research toward clean energy technologies. It has recently been discovered that Ni at low loadings on $CeO_2(111)$ is very active for both of these reactions. Revealing the nature of the active sites in such systems is paramount to a rational design of improved catalysts. Here, we correlate experimental measurements on the $CeO_2(111)$ surface to show that the most active sites are cationic Ni atoms in clusters at step edges, with a small size wherein they have the highest Ni chemical potential. We clarify the reasons for this observation using density functional theory calculations. Focusing on the activation barrier for C−H bond cleavage during the dissociative adsorption of CH_4 as an example, we show that the size and morphology of the supported Ni nanoparticles together with strong Ni-support bonding and charge transfer at the step edge are key to the high catalytic activity. We anticipate that this knowledge will inspire the development of more efficient catalysts for these reactions.

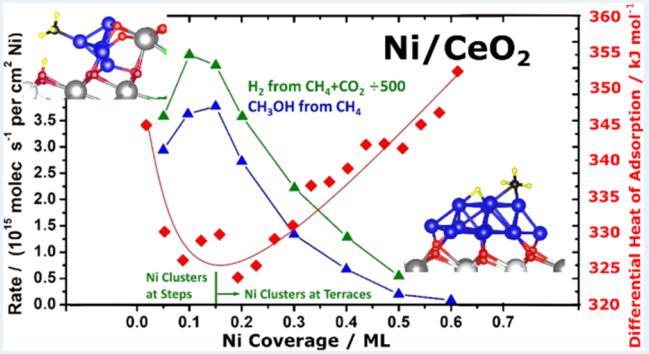

KEYWORDS: *Ni nanoparticles, ceria support, dry reforming, methane to methanol, selective oxidation, metal−support interaction, metal/oxide interface, particle size effect*

INTRODUCTION

The recent dramatic increase in methane availability worldwide has inspired a surge of interest in new catalytic processes for methane conversions that could lead to major environmental and economic benefits. Dry reforming of methane (DRM) is an attractive route that could potentially utilize vast quantities of CO_2 for its catalytic conversion to valuable syngas while simultaneously mitigating both greenhouse gases.[1−4] Perhaps, even more impactful would be the direct catalytic conversion of methane to methanol.[5−9] These two reactions are challenging owing to the high gas-phase stability of their reactants and the rapid deactivation through carbon deposition on high-loaded metal-based catalysts.[10−18] It has been recently shown experimentally[3,4,9,19,20] that small Ni nanoparticles on a ceria(111) model support promote the activation of both O−H and C−H bonds in H_2O and CH_4, respectively, at room temperature, with lower activation barriers than for extended metallic Ni surfaces, and promote the activation of CO_2 at moderate temperatures. Most importantly, this type of catalyst is very active in the DRM in a clean and efficient way[3,4,20] and in the direct conversion of methane to methanol using a mixture of oxygen and water, with a higher selectivity than ever reported for ceria-based catalysts.[9] The activation of CH_4 is the first and only step shared by both reactions, whereas, for example, their steps for C−O bond formation are quite different. In the partial oxidation of methane to methanol, the C−O bond is formed in the addition of chemisorbed CH_3 to O or OH species,[9,13,21,22] whereas in DRM, it is formed from chemisorbed CH and/or C species.[23−27] The high activity of the Ni/CeO_2 catalyst was mainly attributed to the highly cationic character of the interfacial Ni atoms, also reported to be the most active for water−gas shift.[19,27−31] However, a detailed understanding of the structure and nature of the active site remains a challenge and is of paramount importance for the rational development of new or better catalysts. Herein, we report a combination of experimental measurements and density functional theory (DFT) calculations which elucidate the active site, thus hopefully enabling future designs of improved catalysts. We further reveal how this nanomaterial escapes the so-called "tyranny of linear scaling", at least for this

Received: May 12, 2021
Revised: July 23, 2021
Published: August 11, 2021

https://doi.org/10.1021/acscatal.1c02154
ACS Catal. 2021, 11, 10604−10613

key step in these reactions investigated here, namely, methane's dissociative adsorption.

RESULTS

Measurements of Ni Atom Stability and Charge on Ni/CeO_2(111) Correlate with Catalyst Activity. Figure 1

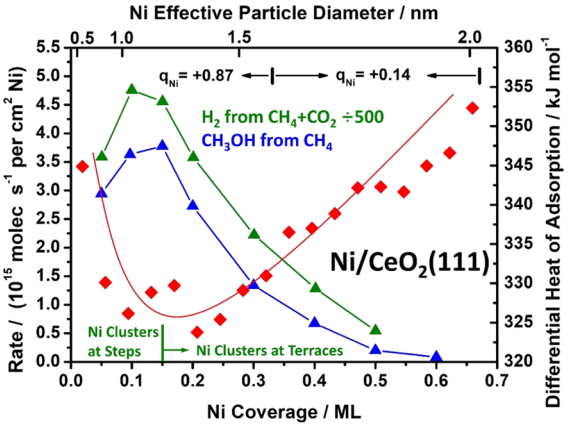

Figure 1. Correlation of the measured catalytic activities versus Ni coverage (and the corresponding average particle size) with Ni atom heat of adsorption for Ni on CeO_2(111). Rates for both methane to methanol at 450 K[9] and methane dry reforming at 650 K[3,20] are shown. The differential heat of Ni adsorption at 300 K[32] shows a minimum when step edges stop being populated by Ni, and Ni bonding at terraces starts to dominate, at the same coverage where both the rates maximize. This coverage corresponds to a Ni particle diameter of ∼1 nm. The average measured charge per Ni atom[32] (shown) also drops strongly near this coverage.

compares the catalytic rate measurements versus Ni loading from two of the abovementioned studies[3,9,20] (blue = CH_3OH from CH_4 and green = DRM) with our recent measurements of the differential heat of adsorption of Ni vapor versus coverage (red). In all cases, these are well-defined model catalysts prepared by vapor-depositing Ni onto the CeO_2(111) support at 300 K, where the support is a nonreduced CeO_2(111) thin film (CeO_{2-x}, with x up to 0.05). These were grown by very similar recipes, on Ru(0001) for the kinetic studies and on Pt(111) for our calorimetry studies. The Ni loading is in ML (defined as the total number of Ni atoms per surface O atom, i.e., 1 ML = 7.89 × 10^{14} atoms per cm^2). The rates are for CH_3OH synthesis from CH_4 (with an 8:1 mix of H_2O + O_2 as the oxidant) at 450 K[9] and DRM at 650 K,[3,20] both at very low conversions. These were originally reported as the rate per unit area of the CeO_2 support (before Ni deposition). We have used the results of our study of this system by low-energy He^+-ion scattering spectroscopy (He^+ LEIS), which gave the ratio of the total Ni area to area of the CeO_2 support versus Ni coverage,[32] to convert these to rates per unit surface area of Ni. This is proportional to the true turnover frequency (TOF, or rate per surface Ni atom), assuming a constant number of Ni surface atoms per unit area of Ni (e.g., 1.6 × 10^{15}/cm^2 for Ni(111) type packing). We also show on the top axis of Figure 1 the average Ni particle's diameter determined from those same LEIS data[32] assuming flat discs with a fixed height/diameter ratio of 0.25, as suggested by scanning tunneling microscopy (STM).[35] These STM measurements were for larger particle sizes than at the rate maximum here (∼1 nm) and possibly missed seeing many or most of the particles smaller than this size due to particle mobility and the limitations of STM imaging on oxide surfaces at the temperature used. Note that dividing the total Ni coverage (in ML) by the fractional area covered by the Ni particles measured by LEIS[32] gives the average Ni particle thickness (in ML, or atoms per unit area, which we converted to nanometers by dividing by the number of Ni atoms per unit volume in bulk Ni(solid) and then converted to particle diameter by dividing by this height/diameter ratio (0.25)). Above 1 nm diameter in Figure 1, the Ni dispersion is approximately equal to 1 nm divided by the diameter.

As seen, the heat of adsorption initially decreases to a minimum and thereafter increases, eventually saturating at the heat of sublimation of bulk Ni(solid), 430 kJ/mol, at higher coverages than shown here.[32] The high initial heat was attributed to the binding of Ni monomers to more stable step edges, and the initial decrease in heat was attributed to the saturation of these step edge sites so that more and more of the less favorable terrace sites are populated with increasing coverage. The heat reaches a minimum and thereafter increases due to the growth of Ni cluster size (reaching ∼2.0 nm on average at the highest coverage shown here).[32] This increase is due to the fact that more Ni−Ni bonds are made to the new Ni atom when it adds to a larger cluster.

Most importantly, in Figure 1, the TOF for both reactions is high and nearly constant with increasing coverage until the minimum heat of adsorption is reached, after which the TOF drops rapidly. This is an outstanding example of a strong correlation between the thermodynamic stability of the metal atoms in a catalyst and its catalytic activity, in this case for two very important reactions. It clearly shows that the active sites are small clusters of Ni at step edges. There is a small increase in TOF at low coverage until it reaches a maximum just at the point where the heat of adsorption reaches a minimum (i.e., where the chemical potential of the Ni atoms in the catalyst reaches a maximum),[32] that is, the most active sites are Ni atoms in clusters at step edges with a small size (∼1.0 nm in diameter and 0.25 nm thick[32]), wherein they have the highest Ni chemical potential.

Note that both these reactions' rates show essentially the same dramatic and complex variation with Ni particle size (coverage). Since the dissociative adsorption of methane is the common step in both reactions, this would suggest that it is the rate-determining step (RDS) in both these reactions under the conditions measured. Although C−O bond forming is also common in both reactions, as mentioned above, in the methanol production reaction, the crucial C−O bond-forming step is the coupling between adsorbed CH_3 with O or OH,[9,13,21,22] whereas this step has not been considered in DFT-based mechanisms for DRM on Ni-based catalysts.[23−27] On Ni(211), a DFT-based microkinetic model of DRM showed that O−CO bond cleavage in CO_2 is the most rate-controlling step (i.e., the one with the highest degree of rate control) under the reaction conditions that led to the highest DRM rates.[33] This step does not occur in the methanol production reaction. It is possible that some later C−O bond-forming step that removes adsorbed carbon atoms (or CH or CH_2) is crucial in both reactions. No one knows yet what is the RDS on the types of sites that are shown above to be the most active for both of these reactions.

Experimentally, it has been observed that this same low coverage of Ni on CeO_2(111) is reactive in dissociating not only CH_4 but also H_2O and CO_2, that is, all the reactants

https://doi.org/10.1021/acscatal.1c02154
ACS Catal. 2021, 11, 10604−10613

involved in both reactions.[3,4,19,20] Thus, an alternate explanation for this similarity in rates versus Ni coverage is that the active site (small Ni clusters at steps) is so much faster than larger Ni clusters in activating all reactants and for both reactions (irrespective of their rate-determining steps) that both rates just track the number of these special sites. Thus, higher Ni coverages just remove these active sites (small Ni clusters) by making them into larger clusters, so that the rates of both reactions go down with Ni coverage in almost exactly the same way. The larger (2 nm) Ni clusters must be >10-fold less active per unit area than the small (1 nm) clusters, if this explanation in true.

We also quantified the charge transfer from Ni to CeO_2(111) versus Ni coverage using X-ray photoelectron spectroscopy (XPS).[32] Figure 1 also shows the measured average charge per added Ni atom (q_{Ni}) in the coverage ranges shown. Upon dosing 1/3 ML, each Ni atom donates nearly one electron to the CeO_2 (making a Ce^{3+}), but above 1/3, there is very little charge transfer and the added Ni is nearly neutral.[32] Our DFT calculations below are consistent with this, showing that small Ni clusters at steps have very cationic Ni, as well as other very special electronic structural properties, and a special ability to activate difficult catalytic reaction steps, using methane activation as an example. They also show that the surface atoms of the larger Ni clusters are nearly neutral in charge, which could explain the lower activity (see also below).

At the Ni coverage where the TOFs in Figure 1 are near their maximum (0.1−0.15 ML), our XPS studies[32] show that a combination of the initial slight extent of reduction of the ceria and the Ni-induced reduction, leads to a surface that is 5−10% Ce^{3+}. This is similar to the fraction of Ce^{3+} measured using *in situ* XPS under DRM reaction conditions at temperatures (600 and 700 K) closest to that used for measuring the TOFs in Figure 1 (650 K).[3,20]

DFT Studies of the Stability and Electronic Character of the Ni/CeO_2(111) Model Catalysts and the Effect of the Support Structure. Our DFT calculations have recently shown that Ni monomers at stoichiometric ⟨110⟩ step edges (Ni_1.step), with a calculated heat of adsorption of 469 kJ/mol, are more strongly bound by 95 kJ/mol[32] than on the flat CeO_2(111) terraces (374 kJ/mol, Figure 2a). In both sites, Ni monomers bind as Ni_1^{2+}. These calculations thus predicted that decoration of the stoichiometric step with Ni species will occur before adsorption on the terraces, as found by our experiments.[32] The maximum possible coverage of monodispersed Ni_1 species at this ⟨110⟩ step edge is three atoms for the unit cell size used there [(5 × 3), corresponding to one Ni for every one step-edge O atoms], with two as Ni_1^{2+} and one as Ni_1^{+} (Figure S1). We calculated the average heat of adsorption of these three coadsorbed Ni_1.step species (460 kJ/mol per atom) and found it to be almost the same as a single step-bound Ni_1, still 86 kJ/mol per Ni atom more strongly bound to the step edge than isolated Ni_1 species on the flat terrace. In our previous work,[32] we have shown that the heat of adsorption of Ni decreases when the step becomes more and more reduced; therefore, oxygen vacancies in the steps were not considered. The size of the unit cell has been chosen to make possible the computationally demanding calculation of the minimum energy path for the dissociative adsorption of methane.

To understand how the ceria step edge affects the electronic structure, charge state, and chemical reactivity of the Ni clusters and their surface atoms, we studied several different

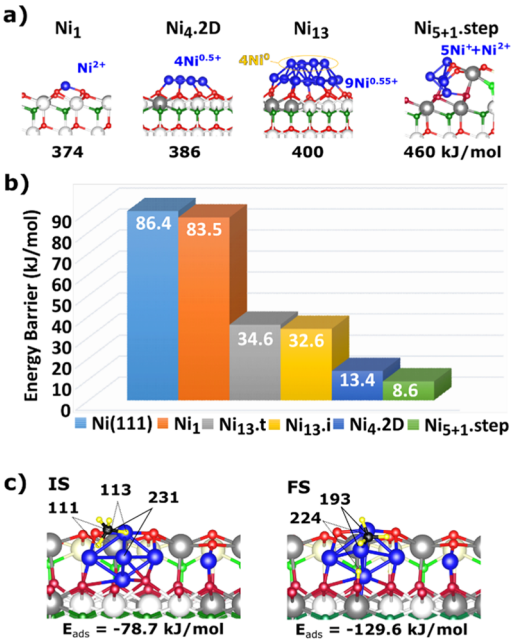

Figure 2. (a) Models of Ni_n (n = 1, 4, and 13) on CeO_2(111) terraces and Ni_5 + Ni_1 (Ni_{5+1}.step) at a ⟨110⟩-type step. Surface/subsurface oxygen atoms in the outermost O−Ce−O trilayer are depicted in red/green, Ce^{4+} is depicted in white, and Ce^{3+} is depicted in gray. Values of the calculated integral heat of adsorption of Ni_n species are listed below each structure in kJ/mol per Ni atom (relative to Ni gas). (Our previous results showed that DFT overpredicts these heats by ∼88 kJ/mol.[32]) (b) Activation energy barriers (non-ZPE-corrected) for the $CH_4 \rightarrow CH_3 + H$ reaction on these Ni_n−CeO_2 systems and for the extended Ni(111) surface. Ni_{13}.t and Ni_{13}.i denote dissociation on a *terrace* and at an *interface* site of the Ni_{13}−CeO_2 system, respectively (cf. Figure 1a). (c) View of the initial state (IS) and final state (FS) for the $CH_4 \rightarrow CH_3 + H$ reaction on the Ni_{5+1}−CeO_2 model catalysts. Selected interatomic distances (in pm) and the adsorption energy of molecularly and dissociatively adsorbed methane (in kJ/mol) are indicated.

representative Ni/CeO_2 structures with DFT. Due to the high computational demands of these studies, we were forced to use smaller clusters than the 1 nm size shown experimentally to be the most active. We chose cluster structures which nevertheless illustrate accurately many of the essential atomic-scale features that control Ni atom stability, electronic structure, and surface reactivity, as described below. These included a small pyramidal Ni_5 cluster (with a rhombohedral base) at the ⟨110⟩ step edge, an isolated Ni_1 adatom, and a flat rhombohedral Ni_4.2D cluster on the ceria terrace, for which all Ni atoms are interfacial, as well as a Ni_{13} cluster which has a two-layered 9−4 stacking structure. A structural Ni_5 isomer was found to be less stable than the pyramidal Ni_5 cluster by 32 kJ/mol, and consequently, it was not considered further (Figure S1). The Ni_{13} cluster has been selected as a representative model that features a compact structure that maximizes the atomic coordination, which makes it particularly likely to be energetically stable. Such a Ni_{13} cluster supported on TiC(001) has recently been used to study the effect of Ni−carbide interactions on the activation of methane.[34]

We first consider the formation of a somewhat larger Ni nanoparticle than we previously studied at the ⟨110⟩ step edge, namely, a pyramid with a rhombohedral base (Ni_5, Figures 2a,c and S1), by adding three more Ni atoms to the fully decorated ⟨110⟩ step with three Ni_1 species. As shown (Figure 2c), two

https://doi.org/10.1021/acscatal.1c02154
ACS Catal. 2021, 11, 10604−10613

of the original Ni atoms are incorporated into the resulting Ni_5 cluster and one remains isolated. This resulting structure has seven Ce^{3+} ions and consists of a pyramidal Ni_5^{5+} nanoparticle and one Ni_1 (Ni_1^{2+}), hereinafter: Ni_{5+1}.step (Figure S1, Table S6). The top atom in this pyramid is the leftmost atom shown in Figure 2a, which, importantly, enables H attachment to the support during H−CH_3 dissociation, as shown below. This step-bound structure has a calculated integral heat of Ni(gas) adsorption that is 66−68 kJ/mol per Ni atom larger than flat Ni_6.2D (392 kJ/mol) or Ni_6.3D (394 kJ/mol) clusters on the $CeO_2(111)$ terrace.[32] This step cluster is also more stable than the rhombohedral Ni_4.2D cluster (which makes 2 Ce^{3+} ions, Figure 2a) and the Ni_{13} aggregate (which makes 5 Ce^{3+} ions), wherein only the four and nine Ni atoms, respectively, in direct contact with the oxide support are partially oxidized (4 × $Ni^{0.50+}$ and 9 × $Ni^{0.56+}$, respectively), whereas the four second-layer Ni atoms in Ni_{13} retain their metallic character (Ni^0). As previously observed,[20,28,32] inspection of the calculated electronic structure for the Ni−CeO_2 systems shown in Figure 1a reveals that the electronic perturbations (e.g., charge transfer) induced by the support are much stronger for Ni atoms which are directly at the Ni−ceria interface, whereas there is almost no charge transfer from the Ni atoms in the second and thicker layers of 3D nanoparticles.[29,35] In contrast, this charge transferred by the Ni atoms is much larger for Ni aggregates at steps and extends to the second Ni layer, that is, the Ni_{5+1}.step structure has a Ni_5^{5+} pyramid with substantial charge even on the top Ni atom and more on the four Ni atoms in the base (totaling +1 charge per Ni, on average) and one Ni^{2+}.

DFT Studies of Methane Activation by Ni−CeO_2 and Linear Scaling Relationships. There is an indisputable correlation between the highest catalytic activity for both methane dry reforming and methane conversion to methanol and the existence of small clusters of nickel dispersed at ceria steps (Figure 1). As noted above, the active low-loaded Ni−CeO_2 systems are much faster not only for both net catalytic reactions than larger Ni clusters but also in dissociating all the reactant gases (CH_4, H_2O, and CO_2). Hence, the positive effects of having small Ni clusters at ceria steps should be reflected in all steps in these reactions. In the following, we test if such sites are indeed particularly active for CH_4 dissociation and consider the activation of the first C−H bond upon CH_4 adsorption on various Ni/$CeO_2(111)$ model catalyst structures, employing the spin-polarized DFT + U approach. Thus, we have calculated the energy profile for methane dissociation at the Ni_{5+1}.step structure shown above and compared that with those on the extended Ni(111) surface,[36] on Ni_1,[36] Ni_4.2D,[36] and Ni_{13} clusters supported on $CeO_2(111)$ terraces. On the Ni_{13} cluster, two Ni sites were considered: one interfacial (i.e., at the perimeter of the Ni cluster) and one on the Ni terrace.

Figure 2b shows that the activation barrier for CH_4 dissociation is the *lowest* among all the clusters and sites modeled for the Ni atom at the apex of the Ni_5 pyramid at a ⟨110⟩ step (8.6 kJ/mol). For the small Ni_4.2D cluster on the CeO_2 terrace with all the Ni atoms being interfacial, the activation barrier for the $CH_4 \rightarrow CH_3$ + H reaction is larger by 4.8 kJ/mol, whereas for interfacial and terrace sites on the Ni_{13} cluster, it is larger by up to 26 kJ/mol.

To shed light on the origin of the activity of ceria-supported Ni clusters, we recall that when dealing with the activation of methane, several descriptors and scaling relations have been examined for the cleavage of the first C−H bond in the hydrocarbon.[37−43] In general, these descriptors and scaling relations provide guidelines to compare and predict the performance of potential new catalysts with that of the existing materials used for C−H bond activation.[37,38,41] Computational volcanos have become important tools in the design of catalysts, and scaling relations are often used in constructing such volcanos and generally considered to have good accuracy.[38,42,44] In the case of methane activation, volcano plots have been presented for metal and/or oxide systems.[38,42,44] For surface-stabilized methane activation pathways, Latimer et al.[38] have proposed a linear Brønsted relation between the energy of the transition state (TS) structure for methane activation, E_{TS} (referenced to gas-phase CH_4 and the clean surface), and that of the FS, $E_{FS} = E_{CH_3+H}$, according to which stronger CH_3 + H binding energies correspond to lower E_{TS} energies, as shown in Figure 3. This model (the red line)

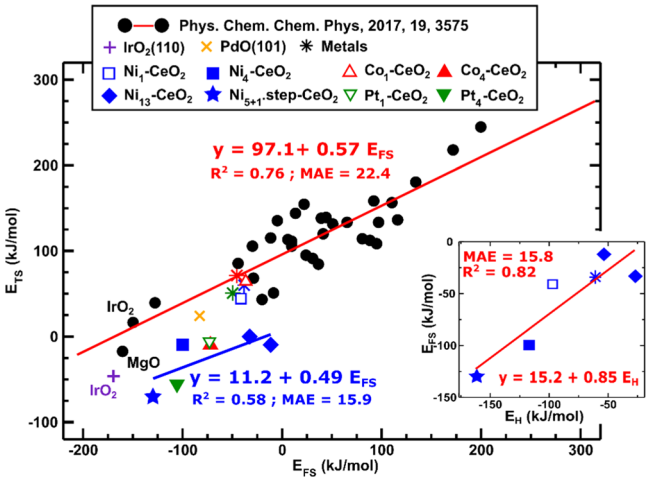

Figure 3. Brønsted relation between the calculated TS and FS energies for the surface-stabilized pathway in methane dissociation on a wide variety of materials. The black dots are for the many systems presented in ref 38, and the red line is the best linear fit reported for these data: $E_{TS} = 0.57E_{FS} + 97.1$. The purple (+) and yellow (×) symbols are for $IrO_2(110)$ and Pd(101) presented in refs 45, 46, and 47, respectively. The green, red, and blue symbols correspond to the E_{TS} and E_{FS} values for M_1 atoms and M_4 clusters (M = Pt, Co, and Ni) on the $CeO_2(111)$, respectively. Values for the extended Pt(111), Co(0001), and Ni(111) surfaces, as in ref 36, and for the Ni_{13} clusters on terraces and Ni_{5+1} at steps are shown. The blue line is the best linear fit for the data corresponding to the Ni_4.2D, Pt_4.2D, Co_4.2D, and Ni_{13} clusters on terraces and Ni_{5+1} at steps. The inset shows the linear relation between the FS binding energy (E_{FS}) and the hydrogen binding energy (E_H) for the nickel-containing catalysts only.

can describe a wide range of materials such as CaO, MgO, PdO, doped MoS_2, and rutile oxides in addition to clean and O- and OH-promoted metals (black dots in Figure 3) with reasonable accuracy. Recently, we have discussed the corresponding results for M_1 atoms and M_4.2D clusters (M = Pt, Co, and Ni) on the $CeO_2(111)$ and on the extended Pt(111), Co(0001), and Ni(111) surfaces.[17] We now include in Figure 3 these results, as well as those for the Ni_{13} cluster on the $CeO_2(111)$ terrace and for the Ni_{5+1}.step at the ⟨110⟩-type step.

Inspection of Figure 3 reveals that the TS energies for the extended Pt, Ni, and Co surfaces and the Ni and Co monomers on $CeO_2(111)$ agree well with the Brønsted

https://doi.org/10.1021/acscatal.1c02154
ACS Catal. 2021, 11, 10604−10613

relation of Latimer et al. However, the TS energies for the Ni clusters on $CeO_2(111)$ are all much lower than its prediction (by 28 to 102 kJ/mol, blue filled square and rhombuses in Figure 3, for values, see Table S2). Importantly, the Ni−CeO_2 system for which the final CH_3 + H state is most strongly bound, namely, the Ni_{5+1}.step at ⟨110⟩ steps (blue filled star), with a FS adsorption energy value of −129.6 kJ/mol (Table S2), has the TS structure of the lowest energy. It is ∼50 kJ/mol below the lowest black point from the original data set of Latimer et al.[38] and ∼57 kJ/mol below its prediction. We note that large deviations below the predicted E_{TS} values also exist for other ceria-supported metal clusters such as Pt_4.2D clusters on the $CeO_2(111)$ terrace (ΔE_{TS} = 84.5 kJ/mol, green filled triangle in Figure 3).[36]

These deviations of the CeO_2-supported Pt nanoparticles from the previous Brønsted relation have recently been explained as a combined effect of the size and morphology of the nanoparticles and strong metal−support interactions, which lead to the stabilization of both the CH_4 molecule (−70 kJ/mol) and the CH_3 + H dissociation product (−105.6 kJ/mol), producing active and stable catalysts for methane activation under very mild conditions.[36] The Pt_4.2D cluster on the $CeO_2(111)$ terrace provides a path for methane activation with a low activation energy barrier of 14.4 kJ/mol that does not involve cooperative interactions between Pt and an O center of the support.

This raises the questions: Can the high reactivity of Ni−ceria systems for methane activation be explained in the same way? Is the Ni_{5+1}.step system unique in some way? When compared not only with all the other Ni−ceria systems investigated (cf. Table S2) but also with Pt_4.2D−ceria,[36] it has the lowest energy barrier for the activation of CH_4 (8.6 kJ/mol, Figure 2b), and its final CH_3 + H state (FS) is the most strongly bound (−129.6 kJ/mol, Figure 3). Its initial adsorbed CH_4 state (IS) is also the most strongly bound (−78.7 kJ/mol). Elucidating the origin of the strong binding of molecularly and dissociatively chemisorbed CH_4 at the Ni_{5+1}.step may provide crucial knowledge on the nature of the active site that enables further improvements on the activity of metal-based catalysts for methane activation.

The dissociation product for the Ni_{5+1}.step, as shown in Figure 2c with CH_3 and H bound to the Ni_5 cluster and to the ceria surface, respectively, reflects that Ni and surface lattice O atoms work in a *cooperative way* to dissociate CH_4 molecules. Such adsorption sites with adjacent Ni and lattice O atoms exist in the low-loaded (∼0.15 ML) active Ni−CeO_2 catalysts for methane conversion[3,4,9] since, as discussed above (Figure 1), for such loadings, Ni binds at step-edge sites. An alternative FS in which both the CH_3 and H species are bound to the Ni_5 cluster is less stable by 123 kJ/mol (Figure S2), and the activation barrier to reach that dissociation product is higher by 75 kJ/mol than that for the path along which lattice O facilitates the dissociation of CH_4 (8.6 kJ/mol). This Ni_{5+1}.step−CeO_2 system is special in this respect. The lowest-barrier path for CH_4 dissociation for the Ni_4.2D and Ni_{13} and Pt_4.2D and Co_4.2D clusters on $CeO_2(111)$ terraces, which also occur with relatively small barriers of 3 to 35 kJ/mol (Table S2 and ref 36), occurs exclusively on the metal atoms and not with the cooperativity found here for this Ni_{5+1}.step−CeO_2 system whereby the H product is bound instead to a lattice O.

We note that a cooperative pathway has also been discussed for dissociation on a Ni_1 adatom on a $CeO_2(111)$ terrace (Figure S2),[3,20] but in this case, the binding of the dissociation product is weaker by 88.3 kJ/mol compared to Ni_{5+1}.step (Table S2). Comparison of the CH_3 + H binding structures for the Ni_1−$CeO_2(111)$ and Ni_{5+1}.step−CeO_2 systems (Figure S3) reveals that the Ni_1 species that adsorbs on a hollow site coordinated to three surface oxygen atoms (Figure 2a) is lifted upon adsorption of the CH_3 species, becoming twofold coordinate instead, which destabilizes the structure. In addition, the distance between the C of the CH_3 group on a Ni site and the H of the formed OH on the ceria support (Figure S3) is by about a factor of 2 smaller (224 pm) for the Ni_{5+1}.step−CeO_2 system as compared to Ni_1 on the ceria terrace (443 pm).

To further stress the argument that it is the cooperativity between the Ni and the ceria support that makes the Ni_{5+1}.step−CeO_2 system special in terms of the ability to stabilize the CH_3 + H products of the first hydrogen abstraction from CH_4, we considered separately the binding of the CH_3 group and that of H on all Ni−ceria systems investigated (Figures S4 and S5). We observed that CH_3 alone on the Ni_4.2D−CeO_2 system is more strongly bound by 14.7 kJ/mol than on Ni_{5+1}.step−CeO_2. However, when the full FS (coadsorbed CH_3 and H) is considered, which for the Ni_{5+1}.step−CeO_2 system implies the formation of OH, the relative stabilities are reversed, with a FS for Ni_{5+1} on ceria steps that is by 29.8 kJ/mol more stable than that for Ni_4.2D clusters on $CeO_2(111)$ terraces (Table S2).

The energy of adsorbed atomic H (wrt 1/2 H_2), calculated by eliminating the CH_3 species from the CH_3 + H FS of all Ni−ceria systems investigated (Figure S4), is the strongest (−162.4 kJ/mol) on an O atom at a terrace site neighboring the step of the Ni_{5+1}.step−CeO_2 system. The inset in Figure 3 shows the existence of a strong linear correlation between the energy of the FS and the binding energy of atomic H, E_H. Hence, the affinity for H can be used as a probe of the local reactivity toward hydrogen abstraction from CH_4. Here, it is important to note that FS structures where the H is on the CeO_2 in the form of an OH species are generally more stable than those where the H species remain on the Ni cluster. However, in most clusters, all such ceria sites are too far from the Ni-bound CH_4 to stabilize the TS for C−H cleavage. The Ni_{5+1}.step−CeO_2 has a special geometry in that respect, which favors the direct "landing" of the abstracted H on the ceria support. In its TS structure, the distance between the H and the lattice O where the O−H bond forms is 252 pm (Figure S3), whereas it is 393 pm for the Ni_4 cluster (cooperative pathway, see Figure S3). Consequently, the activation barrier for this process is 115 kJ/mol higher than that of the path that ends with H on the Ni_4 cluster [128.6 vs 13.4 kJ/mol, see Figure S2].

Note that the strongest CH_3 + H binding energy for Ni_{5+1}.step−CeO_2 among all Ni−ceria systems investigated corresponds to the lowest E_{TS} energy. This is consistent with a linear Brønsted relation for this subset of systems in Figure 3 (the blue line), which is steeper in slope and lies well below the original Brønsted relation there. To shed light into the origin of the large deviation of Ni_{5+1}.step−CeO_2 from the E_{TS} values predicted by that original Brønsted relation (ΔE_{TS} = 56.7 kJ/mol), we inspected the interaction between CH_4 and the Ni_{5+1}.step−CeO_2 system, that is, the IS in the CH_4 to CH_3 + H reaction (Figure 2c). We found that the adsorbed CH_4 molecule is much closer to the surface as compared, for example, to CH_4 on a Ni_1 adatom on a $CeO_2(111)$ terrace

https://doi.org/10.1021/acscatal.1c02154
ACS Catal. 2021, 11, 10604−10613

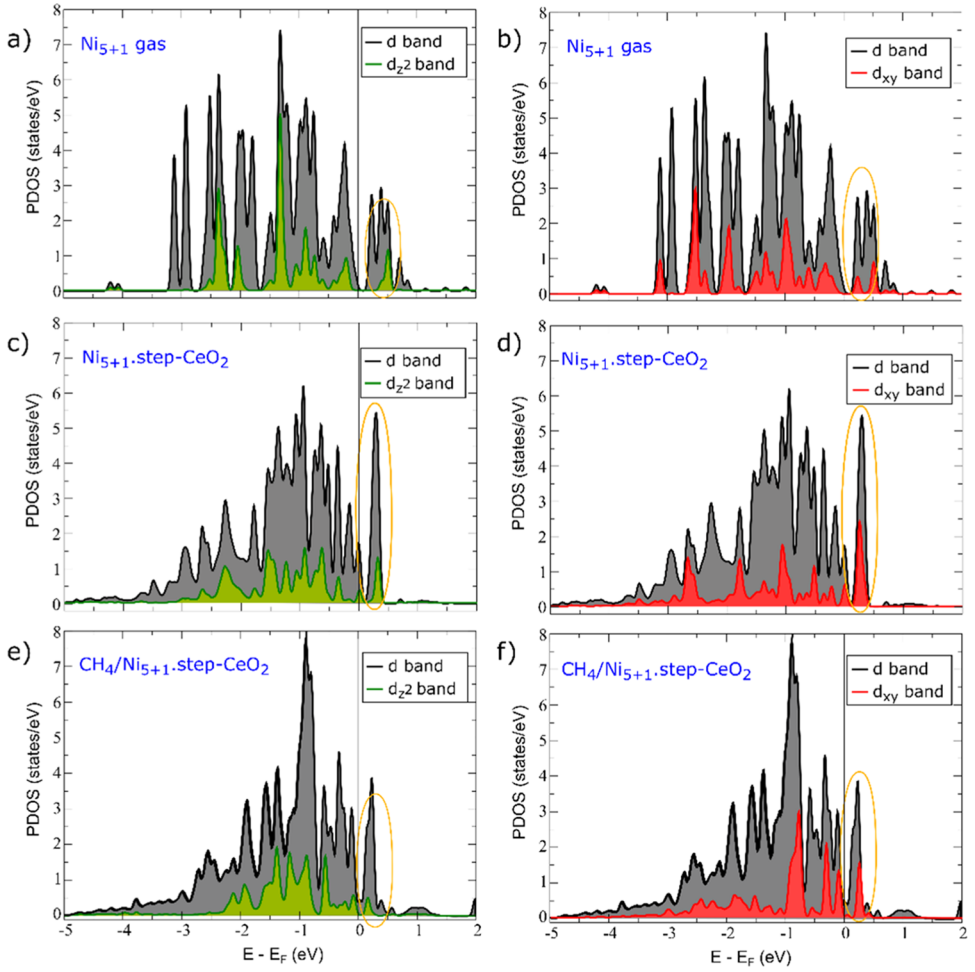

Figure 4. Projected density of states (PDOS) onto the d-states of the Ni atom at the apex of the Ni_5 pyramid of the Ni_{5+1}.step system. The energy zero is the Fermi level (E_F). The green and red filled curves are the corresponding dz^2 and d*xy* projected density of states. (a,b) Results for a free-standing Ni_{5+1} aggregate resulting from the removal of the CeO_2 support from Ni_{5+1}.step−CeO_2, without further geometry optimization, (c,d) results for the Ni_{5+1}.step−CeO_2 system, and (e,f) those for the CH_4 adsorption on Ni_{5+1}.step−CeO_2. The empty states close to E_F are highlighted.

(with C−Ni distances of 231 and 312 pm, respectively). For the Ni_4.2D and Ni_{13} systems, which have activation barriers lower than about 35 kJ/mol (Figure 2b), the CH_4 molecule also binds very close to the surface (with C−Ni distances of 212 (Ni_4.2D), 218 (Ni_{13}.i), and 228 (Ni_{13}.t) pm). For Ni_{5+1}.step−CeO_2 and Ni_4.2D−CeO_2 and Ni_{13}−CeO_2, the direction of electron transfer is to the adsorbed CH_4, as reflected by the increase in the Bader charge for the C atom upon CH_4 adsorption (between 0.11 and 0.16 |e|), with respect to the gas-phase molecule (Table S4); this is not the case for CH_4 adsorption on Ni_1−CeO_2. The important consequence of such a close approach is that the C−H bond that will ultimately be cleaved is already partially activated, with a substantially elongated bond distance, whereas the variation in the other three C−H bonds is almost negligible (Figure S3). This is crucial for the facile dissociation of the first C−H bond on the low-loaded Ni−CeO_2 systems. The case of the Ni_{5+1}.step is shown in Figure 2b where the elongation of one C−H bond upon CH_4 adsorption can clearly be seen. A similarly strong CH_4 adsorption has been recently reported on $Pt_1/TiO_2(110)$,[41] $Pt_4/CeO_2(111)$,[36] and a two-layer-thick PdO(101) film on Pd(100) as compared to a one-layer film.[48] The elongation of one C−H bond upon CH_4 adsorption is reported for all these systems and is accompanied by a significant reduction of the activation barrier for CH_4 dissociation. We further note that for many of the systems in the original set in ref 22, CH_4 is barely or not adsorbed. However, as already mentioned, this is *not* true for some of the metal/CeO_2 systems (nor for $IrO_2(110)$ and Pd(101)), for which the binding of the IS is substantial with one C−H bond partially activated. The best linear fit for the E_{TS} versus E_{FS} data corresponding to the Ni_4.2D, Pt_4.2D, Co_4.2D, and Ni_{13} clusters on terraces and Ni_{5+1} at steps is $E_{TS} = 0.49E_{FS} + 11.2$ (the blue line in Figure 3). We also calculated the best linear fit for the $E_{Barrier}$ versus $E_{Reaction}$ data corresponding to the Ni_4.2D, Pt_4.2D, Co_4.2D, and Ni_{13} clusters on terraces and Ni_{5+1} at steps, $E_{Barrier} = 0.28E_{Reaction} + 26.6$. The comparison of these two linear fits (E_{TS} vs E_{FS} and $E_{Barrier}$ vs $E_{Reaction}$) indicates that about 60% of the slope of the E_{TS} versus E_{FS} regression line is due to a "true" Brønsted relation and about 40% is due to the fact that the FS energy tracks to some extent the IS energy. This 40% is due to the simple fact that metal sites that strongly bind one small C/H containing adsorbate also tend to bind other C/H-containing adsorbates strongly.

To elucidate the reason why CH_4 can get so close to the active Ni_{5+1}.step−CeO_2 system, we inspect first the consequences of the existence of strong metal−support interactions on the d-states of the Ni atom over which CH_4

https://doi.org/10.1021/acscatal.1c02154
ACS Catal. 2021, 11, 10604−10613

dissociates. Figure 4 shows the projected density of states (PDOS) onto the d-states of the Ni atom at the apex of the Ni_5 pyramid for three different cases, namely, the free-standing Ni_{5+1} aggregate resulting from the removal of the CeO_2 support from Ni_{5+1}.step−CeO_2, without further geometry optimization, and the Ni_{5+1}.step−CeO_2 and the CH_4/Ni_{5+1}.step−CeO_2 systems. The detailed analysis of the PDOS (Table S5) reveals that two states, namely, dz^2 and dxy, become less occupied upon adsorption of the Ni_{5+1} aggregate onto the ⟨110⟩ ceria step. The consequence of such a ligand effect is that the Pauli repulsion to the methane's frontier orbital is reduced and the molecule is able to move closer to the surface. These states are then occupied upon CH_4 adsorption as measured by the decrease in the number of empty dz^2 and dxy states in the CH_4/Ni_{5+1}.step−CeO_2 system (Figure 4, Table S5). The electronic perturbation (especially this electron transfer) induced by the binding of Ni to oxygen atoms of the ceria support is important for reactivity toward the first hydrogen abstraction from CH_4 in the Ni_{5+1}.step−CeO_2 system.

We note that a CH_4 molecule that approaches a Ni_1^{2+} adatom on a CeO_2(111) terrace finds the dz^2 state occupied (Figure S8, Table S5), and thus, the repulsion to the frontier methane orbital is larger as compared to the Ni_{5+1}.step−CeO_2 system; consequently, the CH_4 binding is weaker, the C−H bond that will ultimately be cleaved is less elongated, and the deviation between the calculated activation energy barrier and that predicted by the original Brønsted relation is less pronounced.

CONCLUSIONS

Single-crystal adsorption calorimetry and surface analysis measurements (LEIS, XPS, and LEED) combined with DFT calculations have allowed the nature of the active sites in Ni/CeO_2 catalysts for important methane conversions to be identified. The heat of Ni adsorption onto CeO_2(111) at 300 K starts from 345 kJ/mol, decreases within the first 0.15 ML to 323 kJ/mol, and increases afterward. This behavior has been correspondingly attributed to the binding of Ni monomers and small clusters to more stable step edges and the saturation of these step edge sites so that less favorable terrace sites are populated with increasing coverage (and Ni cluster size). A very strong correlation of the heat of adsorption with the catalytic rate measurements versus Ni loading for both the direct conversion of CH_4 to CH_3OH and the CH_4 dry reforming with CO_2 over the Ni−CeO_2(111) catalyst reveals that the activity for both reactions is high and nearly constant with increasing coverage until the minimum heat of adsorption is reached, after which the TOF drops rapidly. This clearly shows that the active sites are small, highly cationic clusters of Ni at CeO_2 step edges, with the highest Ni chemical potential. Moreover, the same coverage of Ni on CeO_2(111) which we show here produces these active sites and was also experimentally shown to be reactive toward dissociative adsorption of all reactants in both reactions. This conclusion is supported by DFT calculations on small Ni clusters on CeO_2(111) terraces and at the ⟨110⟩ step edge that show the lowest energy barrier for the example of CH_4 activation for 2D Ni clusters at this CeO_2 step edge. The calculated H−CH_3 dissociation barrier at this active site drops ∼60 kJ/mol below a previously reported linear scaling relation. Ni−CeO_2 interactions at the step edge lead to stabilization of both the adsorbed CH_4 molecule and its CH_3 + H dissociation product, producing active catalysts. By comparing with other metal−CeO_2 systems, we show that by choosing the "right" metal−oxide combination and manipulating metal−oxide interactions, as well as controlling the structure of the ceria support and the effects of metal loading, an improved activity for methane dissociation can be obtained. Such stabilization by small, non-noble metal clusters at steps of reducible oxide surfaces suggests a promising approach to design efficient catalysts for methane conversion. Moreover, we show that cationic Ni atoms in clusters, with a small size, circumvent the existing linear energy scaling relationship for the cleavage of the first C−H bond in CH_4, which corresponds to the discovery of catalysts following another scaling relationship. This study paves the way for a new way of thinking for the rational design of improved and stable catalysts for methane conversions, a major goal in heterogeneous catalysis.

METHODS

Computational Methods. All electronic structure calculations were carried out using the spin-polarized DFT approach as implemented in the Vienna Ab initio Simulation Package (VASP) [vasp site, http://www.vasp.at; version vasp.5.3.5 and vasp5.4.1].[49,50] Ce (4f, 5s, 5p, 5d, and 6s), O (2s and 2p), and Ni (3p, 3d, and 4s) electrons were explicitly treated as valence states within the projector augmented wave method[51] with a plane-wave cutoff energy of 415 eV, whereas the remaining electrons were considered as part of the atomic core. Total energies and forces were calculated with precisions of 10^{-6} eV and 10^{-2} eV/Å for electronic and force convergence, respectively, within the DFT + U approach by Dudarev et al.[52] ($U_{eff} = U - J = 4.5$ eV for the Ce 4f electrons) with the generalized gradient approximation (GGA) proposed by Perdew, Burke, and Ernzerhof.[53] We note that questions regarding the best value for the U parameter are still under debate.[54−56] Nonetheless, most DFT + U studies of reduced ceria-based systems agree that U values in the range of 4.5−6.0 eV with GGA are suitable for the description of the localization of charge driving the $Ce^{4+} \rightarrow Ce^{3+}$ reduction. However, one should bear in mind that there is, in general, no unique U that gives a reasonable account of all systems' properties.[57−59] Long-range dispersion corrections were also considered, employing the so-called DFT-D3 approach.[60,61] For details on the models and additional computational details, see Supporting Information.

ASSOCIATED CONTENT

Supporting Information

The Supporting Information is available free of charge at https://pubs.acs.org/doi/10.1021/acscatal.1c02154.

Models and computational details; initial, transition, and final states for the $CH_4 \rightarrow CH_3$ + H reaction on ceria-supported Ni clusters; binding of CH_3 and H; Bader charges; projected DOS; and Brønsted relation between the calculated activation barrier and reaction energy (PDF)

AUTHOR INFORMATION

Corresponding Authors

M. Verónica Ganduglia-Pirovano − *Instituto de Catálisis y Petroleoquímica (ICP-CSIC), 28049 Madrid, Spain;* orcid.org/0000-0003-2408-8898; Email: vgp@icp.csic.es

Charles T. Campbell − *Department of Chemistry, University of Washington, Seattle, Washington 98195-1700, United States;* orcid.org/0000-0002-5024-8210; Email: charliec@uw.edu

Authors

Pablo G. Lustemberg − *Instituto de Catálisis y Petroleoquímica (ICP-CSIC), 28049 Madrid, Spain; Instituto de Física Rosario (IFIR-CONICET) and Universidad Nacional de Rosario (UNR), S2000EKF Rosario, Santa Fe, Argentina;* orcid.org/0000-0003-4058-4023

Zhongtian Mao − *Department of Chemistry, University of Washington, Seattle, Washington 98195-1700, United States;* orcid.org/0000-0003-3621-0299

Agustín Salcedo − *Departamento de Ingeniería Química, Facultad de Ingeniería, Universidad de Buenos Aires (UBA), C1428EGA Buenos Aires, Argentina; Instituto de Tecnologías del Hidrógeno y Energías Sostenibles (ITHES, CONICET-UBA), C1428EGA Buenos Aires, Argentina;* orcid.org/0000-0001-5525-8605

Beatriz Irigoyen − *Departamento de Ingeniería Química, Facultad de Ingeniería, Universidad de Buenos Aires (UBA), C1428EGA Buenos Aires, Argentina; Instituto de Tecnologías del Hidrógeno y Energías Sostenibles (ITHES, CONICET-UBA), C1428EGA Buenos Aires, Argentina;* orcid.org/0000-0002-9232-1164

Complete contact information is available at: https://pubs.acs.org/10.1021/acscatal.1c02154

Author Contributions

P.G.L. and Z.M. contributed equally to this work. C.T.C. and M.V.G.-P. designed the study. Z.M. performed the measurements on an apparatus designed by C.T.C., and C.T.C. together with Z.M. wrote the corresponding text in the paper. P.G.L. performed the DFT calculations together with A.S., and M.V.G.-P. together with P.G.L., A.S., and B.I. wrote the corresponding text in the paper. All the authors contributed to the interpretation of the results and commented on the manuscript.

Notes

The authors declare no competing financial interest.

The DFT data that support the findings of this study are available in Materials Cloud {https://www.materialscloud.org/home} with the identifier DOI: 10.24435/materialscloud:ks-qb. The repository contains the calculations described in Figures 2−4 and the related content in Supporting Information. The data are also available from the authors upon reasonable request.

■ ACKNOWLEDGMENTS

The authors (C.T.C. and Z.M.) acknowledge the Department of Energy, Office of Basic Energy Sciences, Chemical Sciences Division grant number DE-FG02-96ER14630, for support of this work. A.S. thanks FIUBA for the Peruilh doctoral fellowship and UBA for the research grant for a short-term stay at the ICP-CSIC in Madrid. This project also received funding from the European Union's Horizon 2020 research and innovation programme under the Marie Skłodowska-Curie grant agreement no 832121. We thank J. A. Rodriguez for helpful discussions. Computer time provided by the Red Española de Supercomputación (RES) resources at MareNostrum 4 (BSC, Barcelona), Caesaraugusta (BIFI-UNIZAR, Zaragoza), and La Palma (IAC, La Laguna, Tenerife) nodes is acknowledged. Computer time provided by the DECI resources at Finis Terrae II based in Spain at CESGA, with the support from PRACE aislb, is also acknowledged. M.V.G.-P. thanks the support by the MICINN-Spain (RTI2018-101604-B-I00).

■ REFERENCES

(1) Akri, M.; Zhao, S.; Li, X.; Zang, K.; Lee, A. F.; Isaacs, M. A.; Xi, W.; Gangarajula, Y.; Luo, J.; Ren, Y.; Cui, Y.-T.; Li, L.; Su, Y.; Pan, X.; Wen, W.; Pan, Y.; Wilson, K.; Li, L.; Qiao, B.; Ishii, H.; Liao, Y.-F.; Wang, A.; Wang, X.; Zhang, T. Atomically Dispersed Nickel as Coke-Resistant Active Sites for Methane Dry Reforming. *Nat. Commun.* **2019**, *10*, 5181.

(2) Song, Y.; Ozdemir, E.; Ramesh, S.; Adishev, A.; Subramanian, S.; Harale, A.; Albuali, M.; Fadhel, B. A.; Jamal, A.; Moon, D.; Choi, S. H.; Yavuz, C. T. Dry reforming of methane by stable Ni-Mo nanocatalysts on single-crystalline MgO. *Science* **2020**, *367*, 777.

(3) Liu, Z.; Grinter, D. C.; Lustemberg, P. G.; Nguyen-Phan, T. D.; Zhou, Y.; Luo, S.; Waluyo, I.; Crumlin, E. J.; Stacchiola, D. J.; Zhou, J.; Carrasco, J.; Busnengo, H. F.; Ganduglia-Pirovano, M. V.; Senanayake, S. D.; Rodriguez, J. A. Dry Reforming of Methane on a Highly-Active Ni-CeO_2 Catalyst: Effects of Metal-Support Interactions on C-H Bond Breaking. *Angew Chem. Int. Ed. Engl.* **2016**, *55*, 7455−7459.

(4) Liu, Z.; Lustemberg, P.; Gutiérrez, R. A.; Carey, J. J.; Palomino, R. M.; Vorokhta, M.; Grinter, D. C.; Ramírez, P. J.; Matolín, V.; Nolan, M.; Ganduglia-Pirovano, M. V.; Senanayake, S. D.; Rodriguez, J. A. In Situ Investigation of Methane Dry Reforming on Metal/Ceria(111) Surfaces: Metal-Support Interactions and C−H Bond Activation at Low Temperature. *Angew Chem. Int. Ed. Engl.* **2017**, *56*, 13041−13046.

(5) Liu, Z.; Huang, E.; Orozco, I.; Liao, W.; Palomino, R. M.; Rui, N.; Duchoň, T.; Nemšák, S.; Grinter, D. C.; Mahapatra, M.; Liu, P.; Rodriguez, J. A.; Senanayake, S. D. Water-Promoted Interfacial Pathways in Methane Oxidation to Methanol on a CeO_2-Cu_2O Catalyst. *Science* **2020**, *368*, 513.

(6) Jin, Z.; Wang, L.; Zuidema, E.; Mondal, K.; Zhang, M.; Zhang, J.; Wang, C.; Meng, X.; Yang, H.; Mesters, C.; Xiao, F.-S. Hydrophobic Zeolite Modification for in Situ Peroxide Formation in Methane Oxidation to Methanol. *Science* **2020**, *367*, 193.

(7) Tang, Y.; Li, Y.; Fung, V.; Jiang, D.-e.; Huang, W.; Zhang, S.; Iwasawa, Y.; Sakata, T.; Nguyen, L.; Zhang, X.; Frenkel, A. I.; Tao, F. Single Rhodium Atoms Anchored in Micropores for Efficient Transformation of Methane Under Mild Conditions. *Nat. Commun.* **2018**, *9*, 1231.

(8) Xie, J.; Jin, R.; Li, A.; Bi, Y.; Ruan, Q.; Deng, Y.; Zhang, Y.; Yao, S.; Sankar, G.; Ma, D.; Tang, J. Highly Selective Oxidation of Methane to Methanol at Ambient Conditions by Titanium Dioxide-Supported Iron species. *Nat. Catal.* **2018**, *1*, 889−896.

(9) Lustemberg, P. G.; Palomino, R. M.; Gutiérrez, R. A.; Grinter, D. C.; Vorokhta, M.; Liu, Z.; Ramírez, P. J.; Matolín, V.; Ganduglia-Pirovano, M. V.; Senanayake, S. D.; Rodriguez, J. A. Direct Conversion of Methane to Methanol on Ni-Ceria Surfaces: Metal-Support Interactions and Water-Enabled Catalytic Conversion by Site Blocking. *J. Am. Chem. Soc.* **2018**, *140*, 7681−7687.

(10) Meng, X.; Cui, X.; Rajan, N. P.; Yu, L.; Deng, D.; Bao, X. Direct Methane Conversion under Mild Condition by Thermo-, Electro-, or Photocatalysis. *Chem* **2019**, *5*, 2296−2325.

(11) Cui, X.; Huang, R.; Deng, D. Catalytic Conversion of C1 Molecules under Mild Conditions. *EnergyChem* **2021**, *3*, 100050.

(12) Senanayake, S. D.; Rodriguez, J. A.; Weaver, J. F. Low Temperature Activation of Methane on Metal-Oxides and Complex Interfaces: Insights from Surface Science. *Acc. Chem. Res.* **2020**, *53*, 1488−1497.

(13) Latimer, A. A.; Kakekhani, A.; Kulkarni, A. R.; Nørskov, J. K. Direct Methane to Methanol: The Selectivity-Conversion Limit and Design Strategies. *ACS Catal.* **2018**, *8*, 6894−6907.
(14) Pakhare, D.; Spivey, J. A Review of Dry (CO_2) Reforming of Methane over Noble Metal Catalysts. *Chem. Soc. Rev.* **2014**, *43*, 7813−7837.
(15) Horn, R.; Schlögl, R. Methane Activation by Heterogeneous Catalysis. *Catal. Lett.* **2015**, *145*, 23−39.
(16) Schwarz, H.; Shaik, S.; Li, J. Electronic Effects on Room-Temperature, Gas-Phase C-H Bond Activations by Cluster Oxides and Metal Carbides: The Methane Challenge. *J. Am. Chem. Soc.* **2017**, *139*, 17201−17212.
(17) Fan, C.; Zhu, Y.-A.; Yang, M.-L.; Sui, Z.-J.; Zhou, X.-G.; Chen, D. Density Functional Theory-Assisted Microkinetic Analysis of Methane Dry Reforming on Ni Catalyst. *Ind. Eng. Chem. Res.* **2015**, *54*, 5901−5913.
(18) Choudhary, T. V.; Goodman, D. W. Methane Activation on Ni and Ru Model Catalysts. *J. Mol. Catal. A: Chem.* **2000**, *163*, 9−18.
(19) Carrasco, J.; López-Durán, D.; Liu, Z.; Duchoň, T.; Evans, J.; Senanayake, S. D.; Crumlin, E. J.; Matolín, V.; Rodríguez, J. A.; Ganduglia-Pirovano, M. V. In Situ and Theoretical Studies for the Dissociation of Water on an Active Ni/CeO_2 Catalyst: Importance of Strong Metal-Support Interactions for the Cleavage of O-H Bonds. *Angew. Chem., Int. Ed.* **2015**, *54*, 3917−3921.
(20) Lustemberg, P. G.; Ramírez, P. J.; Liu, Z.; Gutiérrez, R. A.; Grinter, D. G.; Carrasco, J.; Senanayake, S. D.; Rodriguez, J. A.; Ganduglia-Pirovano, M. V. Room-Temperature Activation of Methane and Dry Re-forming with CO_2 on Ni-CeO_2(111) Surfaces: Effect of Ce^{3+} Sites and Metal−Support Interactions on C−H Bond Cleavage. *ACS Catal.* **2016**, *6*, 8184−8191.
(21) Gannouni, A.; Delbecq, F.; Saïd Zina, M.; Sautet, P. Oxidation of Methane to Methanol over Single Site Palladium Oxide Species on Silica: A Mechanistic view from DFT. *J. Phys. Chem. A* **2017**, *121*, 5500−5508.
(22) Wen, J.-H.; Guo, D.; Wang, G.-C. Structure-Sensitivity of Direct Oxidation Methane to Methanol over Rh_n/ZrO_{2-x} (101) (n = 1, 4, 10) Surfaces: A DFT Study. *Appl. Surf. Sci.* **2021**, *555*, 149690.
(23) Wang, S.-G.; Cao, D.-B.; Li, Y.-W.; Wang, J.; Jiao, H. CO_2 Reforming of CH_4 on Ni(111): A Density Functional Theory Calculation. *J. Phys. Chem. B* **2006**, *110*, 9976−9983.
(24) Zhu, Y.-A.; Chen, D.; Zhou, X.-G.; Yuan, W.-K. DFT Studies of Dry Reforming of Methane on Ni Catalyst. *Catal. Today* **2009**, *148*, 260−267.
(25) Wang, Z.; Cao, X.-M.; Zhu, J.; Hu, P. Activity and Coke Formation of Nickel and Nickel Carbide in Dry Reforming: A Deactivation Scheme from Density Functional Theory. *J. Catal.* **2014**, *311*, 469−480.
(26) Guo, Y.; Feng, J.; Li, W. Effect of the Ni Size on CH_4/CO_2 Reforming over Ni/MgO Catalyst: A DFT Study. *Chin. J. Chem. Eng.* **2017**, *25*, 1442−1448.
(27) Lian, Z.; Olanrele, S. O.; Si, C.; Yang, M.; Li, B. Critical Role of Interfacial Sites between Nickel and CeO_2 Support in Dry Reforming of Methane: Revisit of Reaction Mechanism and Origin of Stability. *J. Phys. Chem. C* **2020**, *124*, 5118−5124.
(28) Carrasco, J.; Barrio, L.; Liu, P.; Rodriguez, J. A.; Ganduglia-Pirovano, M. V. Theoretical Studies of the Adsorption of CO and C on Ni(111) and Ni/CeO_2(111): Evidence of a Strong Metal−Support Interaction. *J. Phys. Chem. C* **2013**, *117*, 8241−8250.
(29) Senanayake, S. D.; Evans, J.; Agnoli, S.; Barrio, L.; Chen, T.-L.; Hrbek, J.; Rodriguez, J. A. Water−Gas Shift and CO Methanation Reactions over Ni−CeO_2(111) Catalysts. *Top. Catal.* **2011**, *54*, 34−41.
(30) Lustemberg, P. G.; Feria, L.; Ganduglia-Pirovano, M. V. Single Ni Sites Supported on CeO_2(111) Reveal Cooperative Effects in the Water−Gas Shift Reaction. *J. Phys. Chem. C* **2018**, *123*, 7749−7757.
(31) Singha, R. K.; Tsuji, Y.; Mahyuddin, M. H.; Yoshizawa, K. Methane Activation at the Metal−Support Interface of Ni_4−CeO_2(111) Catalyst: A Theoretical Study. *J. Phys. Chem. C* **2019**, *123*, 9788−9798.
(32) Mao, Z.; Lustemberg, P. G.; Rumptz, J. R.; Ganduglia-Pirovano, M. V.; Campbell, C. T. Ni Nanoparticles on CeO_2(111): Energetics, Electron Transfer, and Structure by Ni Adsorption Calorimetry, Spectroscopies, and Density Functional Theory. *ACS Catal.* **2020**, *10*, 5101−5114.
(33) Chen, S.; Zaffran, J.; Yang, B. Descriptor Design in the Computational Screening of Ni-Based Catalysts with Balanced Activity and Stability for Dry Reforming of Methane Reaction. *ACS Catal.* **2020**, *10*, 3074−3083.
(34) Prats, H.; Gutiérrez, R. A.; Piñero, J. J.; Viñes, F.; Bromley, S. T.; Ramírez, P. J.; Rodriguez, J. A.; Illas, F. Room Temperature Methane Capture and Activation by Ni Clusters Supported on TiC(001): Effects of Metal-Carbide Interactions on the Cleavage of the C-H Bond. *J. Am. Chem. Soc.* **2019**, *141*, 5303−5313.
(35) Zhou, Y.; Zhou, J. Interactions of Ni Nanoparticles with Reducible CeO_2(111) Thin Films. *J. Phys. Chem. C* **2012**, *116*, 9544−9549.
(36) Lustemberg, P. G.; Zhang, F.; Gutiérrez, R. A.; Ramírez, P. J.; Senanayake, S. D.; Rodriguez, J. A.; Ganduglia-Pirovano, M. V. Breaking Simple Scaling Relations through Metal−Oxide Interactions: Understanding Room-Temperature Activation of Methane on M/CeO_2 (M = Pt, Ni, or Co) Interfaces. *J. Phys. Chem. Lett.* **2020**, *11*, 9131−9137.
(37) Aljama, H.; Nørskov, J. K.; Abild-Pedersen, F. Tuning Methane Activation Chemistry on Alkaline Earth Metal Oxides by Doping. *J. Phys. Chem. C* **2018**, *122*, 22544−22548.
(38) Latimer, A. A.; Aljama, H.; Kakekhani, A.; Yoo, J. S.; Kulkarni, A.; Tsai, C.; Garcia-Melchor, M.; Abild-Pedersen, F.; Nørskov, J. K. Mechanistic Insights into Heterogeneous Methane Activation. *Phys. Chem. Chem. Phys.* **2017**, *19*, 3575−3581.
(39) Weaver, J. F.; Hakanoglu, C.; Antony, A.; Asthagiri, A. Alkane Activation on Crystalline Metal Oxide Surfaces. *Chem. Soc. Rev.* **2014**, *43*, 7536−7547.
(40) Tsuji, Y.; Yoshizawa, K. Adsorption and Activation of Methane on the (110) Surface of Rutile-type Metal Dioxides. *J. Phys. Chem. C* **2018**, *122*, 15359−15381.
(41) Fung, V.; Tao, F.; Jiang, D.-e. Low-Temperature Activation of Methane on Doped Single Atoms: Descriptor and Prediction. *Phys. Chem. Chem. Phys.* **2018**, *20*, 22909−22914.
(42) Latimer, A. A.; Kulkarni, A. R.; Aljama, H.; Montoya, J. H.; Yoo, J. S.; Tsai, C.; Abild-Pedersen, F.; Studt, F.; Nørskov, J. K. Understanding Trends in C-H Bond Activation in Heterogeneous Catalysis. *Nat. Mater.* **2017**, *16*, 225−229.
(43) Ma, X.; Sun, K.; Liu, J.-X.; Li, W.-X.; Cai, X.; Su, H.-Y. Single Ru Sites-Embedded Rutile TiO_2 Catalyst for Non-Oxidative Direct Conversion of Methane: A First-Principles Study. *J. Phys. Chem. C* **2019**, *123*, 14391−14397.
(44) Pérez-Ramírez, J.; López, N. Strategies to Break Linear Scaling Relationships. *Nat. Catal.* **2019**, *2*, 971−976.
(45) Kim, M.; Franklin, A.; Martin, R.; Feng, F.; Li, T.; Liang, Z.; Asthagiri, A.; Weaver, J. F. Adsorption and Oxidation of CH_4 on Oxygen-Rich IrO_2(110). *J. Phys. Chem. C* **2019**, *123*, 27603−27614.
(46) Liang, Z.; Li, T.; Kim, M.; Asthagiri, A.; Weaver, J. F. Low-Temperature Activation of Methane on the IrO_2(110) Surface. *Science* **2017**, *356*, 299−303.
(47) Antony, A.; Asthagiri, A.; Weaver, J. F. Pathways and Kinetics of Methane and Ethane C-H bond Cleavage on PdO(101). *J. Chem. Phys.* **2013**, *139*, 104702.
(48) Martin, N. M.; Van den Bossche, M.; Hellman, A.; Grönbeck, H.; Hakanoglu, C.; Gustafson, J.; Blomberg, S.; Johansson, N.; Liu, Z.; Axnanda, S.; Weaver, J. F.; Lundgren, E. Intrinsic Ligand Effect Governing the Catalytic Activity of Pd Oxide Thin Films. *ACS Catal.* **2014**, *4*, 3330−3334.
(49) Kresse, G.; Hafner, J. Ab initiomolecular dynamics for liquid metals. *Phys. Rev. B: Condens. Matter Mater. Phys.* **1993**, *47*, 558−561.
(50) Kresse, G.; Furthmüller, J. Efficient iterative schemes forab initiototal-energy calculations using a plane-wave basis set. *Phys. Rev. B: Condens. Matter Mater. Phys.* **1996**, *54*, 11169−11186.

https://doi.org/10.1021/acscatal.1c02154
ACS Catal. 2021, 11, 10604−10613

(51) Kresse, G.; Joubert, D. From Ultrasoft Pseudopotentials to the Projector Augmented-Wave Method. *Phys. Rev. B: Condens. Matter Mater. Phys.* **1999**, *59*, 1758−1775.
(52) Dudarev, S. L.; Botton, G. A.; Savrasov, S. Y.; Humphreys, C. J.; Sutton, A. P. Electron-Energy-Loss Spectra and the Structural Stability of Nickel Oxide: An LSDA+U Study. *Phys. Rev. B: Condens. Matter Mater. Phys.* **1998**, *57*, 1505−1509.
(53) Perdew, J. P.; Burke, K.; Ernzerhof, M. Generalized Gradient Approximation Made Simple. *Phys. Rev. Lett.* **1996**, *77*, 3865−3868.
(54) Fabris, S.; Vicario, G.; Balducci, G.; de Gironcoli, S.; Baroni, S. Electronic and Atomistic Structures of Clean and Reduced Ceria Surfaces. *J. Phys. Chem. B* **2005**, *109*, 22860−22867.
(55) Castleton, C. W. M.; Kullgren, J.; Hermansson, K. Tuning LDA +U for Electron Localization and Structure at Oxygen Vacancies in Ceria. *J. Chem. Phys.* **2007**, *127*, 244704.
(56) Andersson, D. A.; Simak, S. I.; Johansson, B.; Abrikosov, I. A.; Skorodumova, N. V. Modeling of CeO_2, Ce_2O_3, and CeO_{2-x} in the LDA+U Formalism. *Phys. Rev. B: Condens. Matter Mater. Phys.* **2007**, *75*, 035109.
(57) Da Silva, J. L. F.; Ganduglia-Pirovano, M. V.; Sauer, J.; Bayer, V.; Kresse, G. Hybrid Functionals Applied to Rare-Earth Oxides: The Example of Ceria. *Phys. Rev. B: Condens. Matter Mater. Phys.* **2007**, *75*, 045121.
(58) Du, D.; Wolf, M. J.; Hermansson, K.; Broqvist, P. Screened Hybrid Functionals Applied to Ceria: Effect of Fock Exchange. *Phys. Rev. B* **2018**, *97*, 235203.
(59) Loschen, C.; Carrasco, J.; Neyman, K. M.; Illas, F. First-Principles LDA+U and GGA+U Study of Cerium Oxides: Dependence on the Effective U Parameter. *Phys. Rev. B: Condens. Matter Mater. Phys.* **2007**, *75*, 035115.
(60) Grimme, S.; Antony, J.; Ehrlich, S.; Krieg, H. A Consistent and Accurate Ab Initio Parametrization of Density Functional Dispersion Correction (DFT-D) for the 94 elements H-Pu. *J. Chem. Phys.* **2010**, *132*, 154104.
(61) Grimme, S.; Ehrlich, S.; Goerigk, L. Effect of the Damping Function in Dispersion Corrected Density Functional Theory. *J. Comput. Chem.* **2011**, *32*, 1456−1465.

https://doi.org/10.1021/acscatal.1c02154
ACS Catal. 2021, 11, 10604−10613